CHAPTER: 3

Studies on Structural, Morphological, and Electrical Properties of Ga^{3+} and Cu^{2+} co-doped Ceria Ceramics as Solid Electrolyte for IT-SOFCs

3.1 Introduction

The solid electrolyte is the key component in determining performance of SOFCs as it facilitates the migration of oxygen ions from one electrode to another electrode [Ji et al., 2015]. Conventionally, YSZ (yttrium stabilized zirconia) has been most widely accepted electrolyte for SOFC applications in higher temperature region (~1000°C) [Yamamoto et al., 1995]. Nevertheless, the need of its high operating temperature restricts the selection of materials for various components, durability and commercialization. Considerable attempts have been made to overcome these issues by developing alternative electrolytes with low operating temperatures. Moreover, an ideal electrolyte should also have high oxide ion conductivity, thermal stability over a broad temperature range, and chemical compatibility in oxidizing and reducing atmospheres [Bhabu et al., 2016; Kuang et al., 2008; Wei et al., 2015]. In this regard, alkaline earth, rare earth metal and transition metal doped ceria based solid electrolytes have fascinated considerable research interest owing to their relatively low operating temperatures and high oxide ion conductivity as compared to other traditional electrolytes and also the undoped ceria [Anirban et al., 2015; Kahlaoui et al., 2016]. However, the necessity of high sintering temperature of ceria based doped materials poses notable problems such as partial reduction of Ce^{4+} into Ce^{3+} which increases electronic conductivity. High manufacturing cost and extensive segregation of defect cluster which deteriorates the grain boundary conductivity via blocking of oxygen ion diffusion through the interfaces of the grain boundaries are also associated with the high sintering temperature [Lima et al., 2015; Sudarsan et al. 2018; Dong et al., 2011]. Two important aspects that lead to the blocking of oxygen ion diffusion at grain boundaries are: (i) segregation of siliceous impurity in grain boundary through low impurity precursors during high temperature sintering, and (ii) formation of space charge layer acting as barrier for migration of negative oxygen ion by inducing a reduction of positively charged oxygen vacancy in grain boundary core [Guo et al., 2006; Zhang et al., 2004; Kim et al., 2002; Tuller et al., 2000]. Herle et al. have reported that co-doping or multiple ion doping in ceria results into higher oxide ion conductivity as it can suppress the ordering of oxygen vacancies [Herle et al., 1999]. Further, the co-doping is also beneficial in conquering the electronic conduction of CeO_2 in reducing atmosphere. In view of this, proper investigation of suitable dopants and sintering aid with optimum concentration on co-doping scheme is essential for improving the conduction behaviour of cerium oxide for potential electrolyte applications [Venkataramana et al., 2017; Wu et al., 2014]. To the best our knowledge, there has been no study investigating the effect of Ga^{3+} and Cu^{2+} co-doping on the structure, microstructure, and electrical properties of ceria for SOFCs applications. In this chapter, I report the results of our studies on novel co-doped $Ce_{0.8}Ga_{0.2-x}Cu_xO_{2-\delta}$ ($0\leq x \geq 0.2$) nanopowders prepared by using auto combustion method. Various compositions of the developed electrolyte material have been characterized for the crystal structure, thermal behavior, morphology and electrical properties using XRD, TGA, SEM, TEM and impedance measurements.

3.2 Experimental Section

3.2.1 Materials Preparation

All the compositions of Ga^{3+} and Cu^{2+} co-doped ceria nanopowders $Ce_{0.8}Ga_{0.2-x}Cu_xO_{2-\delta}$ (x=0, 0.05, 0.1, 0.15, 0.2) have been prepared by auto combustion synthesis using glycine as fuel. These compositions are designated as G20C0, G15C5, G10C10, G5C15 and G0C20, respectively, in following discussions. In the synthesis process, stoichiometric amounts of CeO_2, $Ga(NO_3)_3$, CuO were used as starting materials. At first, CeO_2 and CuO were dissolved in dilute nitric acid along with de-ionized water, followed by heating at 100°C. After that de-ionized water were used to dissolve

$Ga(NO_3)_3$ along with glycine. Subsequently, all the prepared solutions were mixed together and heated on a hot plate at ~300°C with continuous stirring. The solvent evaporated after 7-8 hrs resulting into highly viscous gel. After a few minutes, auto-ignition started due to exothermic combustion reaction throughout the sample, leading to fine nanopowder. Typical exothermic combustion reaction in the process is given by the following equation:

$$0.8Ce(NO_3)_4 + (0.2\text{-}x)Ga(NO_3)_3 + xCu(NO_3)_2 + C_2H_5NO_2 + O_2 \rightarrow Ce_{0.8}Ga_{0.2\text{-}x}Cu_xO_{2\text{-}\delta} + N_2 + CO_2 + H_2O \qquad \text{Eq. 3.1}$$

The as synthesized $Ce_{0.8}Ga_{0.2\text{-}x}Cu_xO_{2\text{-}\delta}$ powders were calcined for 2 h at 700°C in order to remove volatile components left and then calcined powders were crushed by grinding in an agate mortar. The hydraulic press was used to press the powders at 70 MPa in to cylindrical pellets having a diameter 10 mm and thickness 2mm. The obtained pellets were subsequently sintered for 4 h at 1300° C in SiC furnace.

3.2.2 Characterization

The phase purity and crystal structure of the calcined powders were characterized by Rigaku high resolution powder X-ray diffractometer (λ=1.5406Å/ CuKα) with step width of 0.02° over a 2θ range from 20° to 100°. The average crystallite sizes of all the calcined nanopowders were obtained by using Debye Scherrer’s equation given below.

$$D = K\lambda/\beta\cos\theta \qquad \text{Eq. 3.2}$$

where β is the full width at half maxima (FWHM) of the most intense Bragg peak of XRD pattern, K is the shape factor, θ is the Bragg angle, λ is the wavelength of incident X-rays. The relative density of sintered pellets was calculated by the following equation

$$D_{rel}\,(\%) = D_{exp.}/D_{th.} \times 100 \qquad \text{Eq. 3.3}$$

where $D_{exp.}$ is the measured apparent density (mass/volume) and D_{th}. is the theoretical density calculated by XRD data employing Rietveld refinement. Thermal behavior of prepared solid electrolyte materials were investigated by using Mettler Toledo thermogravimetric and differential thermal analysis (TGA/DTA) analysis in the temperature range 40 to 800°C with heating rate 10 °Cmin^{-1}. The homogeneity and phase structural study of the samples were investigated by using Raman spectroscopy (STR-300) over the frequency range of 200 cm^{-1} to 1000 cm^{-1}. The microstructural measurements and energy dispersive spectroscopic (EDS) analysis of the sintered pellets were carried out by scanning electron microscopy (ZEISS EVO 18). Transmission electron microscopy (Tecnai G2 20 TWIN) was used to characterize the average particle size of $Ce_{0.8}Ga_{0.05}Cu_{0.15}O_{1.825}$ nanopowders. For electrical measurements, silver contacts were applied on both the flat surfaces of sintered pellets followed by curing at 500°C for 15 min. An impedance analyzer (KEYSIGHT-E4990A) was used to characterize the impedance spectra of sintered samples in static ambient atmosphere in the frequency range 20Hz to 5MHz from 200 to 700°C. To determine the ionic conductivity of electrolytes, the impedance data were fitted to equivalent electronic circuit using Z-Simpwin software. The thermal expansion measurements on samples were done by high temperature X-ray diffraction (HT-XRD) data using Rigaku Smart Lab 9kW Powder diffractometer.

3.3 Results and Discussion:

3.3.1 Powder X-ray Diffraction

Figure 3.1a shows the room temperature XRD patterns of calcined $Ce_{0.8}Ga_{0.2-x}Cu_xO_{2-\delta}$ samples with x=0, 0.05, 0.1, 0.15, and 0.2. Comparison of the XRD patterns of co-doped compositions with pure CeO_2 (JCPDS Card No.-34-0394) suggests that they are nearly single phase and iso-structural to pure cerium oxide with cubic fluorite structure similar to CeO_2 having space group F*m-3m*. In addition, compositions with x=0.1, 0.15, 0.2 exhibit two weak peaks around 35.5° and 38.8°, which can be attributed to a monoclinic CuO (JCPDS Card No.-89-5895) phase. The solubility of CuO in cerium oxide is limited because of the different ionic size and crystal structures which leads to the segregation of CuO in solid solution for higher compositions (x>0.05). The Rietveld refinement of the crystal structure confirms the cubic crystal structure of co-doped nanocrystalline samples obtained after calcination.

The Rietveld fits for the XRD patterns of $Ce_{0.8}Ga_{0.2-x}Cu_xO_{2-\delta}$ samples with x=0, 0.05, 0.1, 0.15, and 0.2 are presented in Figure 3.2. As can be seen from this figure, the Rietveld fits are very good for the XRD patterns of co-doped ceria samples. Table 3.1 list the lattice parameter and unit cell volume determined from the Rietveld structure refinement. It also lists the relative density and crystallite size for different compositions. It is evident that with increasing Cu concentration, the lattice parameter, crystallite size and unit cell volume show increasing trend. The substitution of smaller Ga-ions (ionic radius 0.62 Å) by larger size Cu-ions (ionic radius 0.73 Å) is expected to increase the lattice parameter. The solid solubility limit of CuO in ceria is around 0.1%. Once CuO content go beyond this solubility limit the excess CuO segregate to the grain boundaries. This suggests that the cell parameter should not change for the doping concentration of CuO beyond 0.1%. As given in Table 3.1, the cell parameters of the compositions G10C10 and G0C20 are indeed nearly comparable. The slight decrease in the cell parameter for the x=0.15, composition (0.001Å) may be linked with formation of slightly excess CuO precipitate in this composition. A graphical plot for the lattice parameter and crystallite size for $Ce_{0.8}Ga_{0.2-x}Cu_xO_{2-\delta}$ samples is shown in Figure 3.1b. The average crystallite size of the calcined powders of co-doped samples calculated from Scherrer's formula was also found to increase continuously with CuO doping as depicted in this figure. This can be ascribed to the lower melting point CuO assisted liquid phase sintering, leading to the larger grains for higher CuO concentrations. The relative density of the samples is also found to increase with CuO doping which further confirms the presence of liquid phase sintering in these samples.

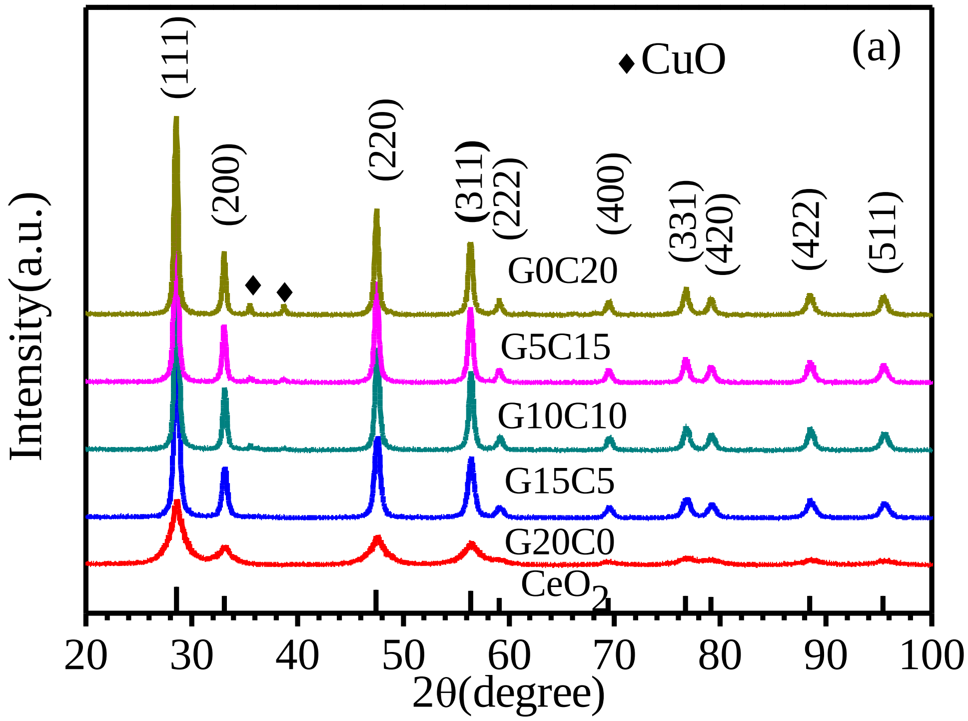

Figure 3.1 (a) Powder X-Ray diffraction patterns of the $Ce_{0.8}Ga_{0.2-x}Cu_xO_{2-\delta}$ (x=0, 0.05, 0.1, 0.15, 0.2) samples at room temperature. The reference peak positions for pure CeO_2 are also marked at the bottom.

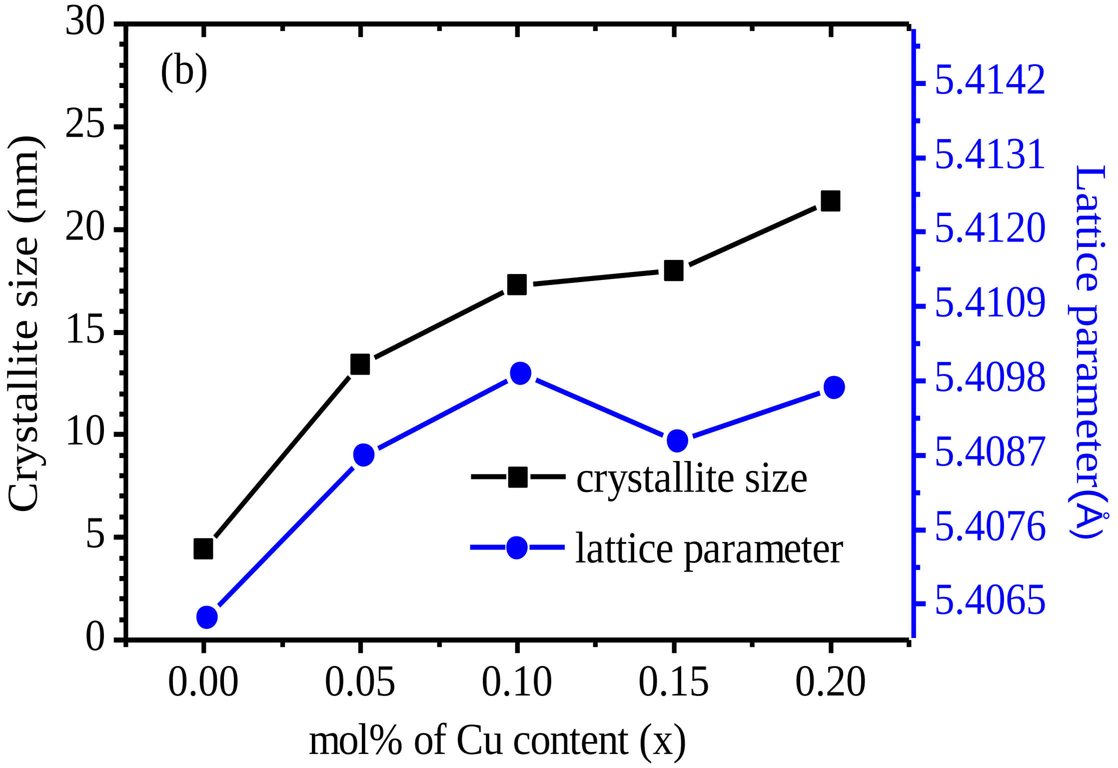

Figure 3.1 (b) Variation of lattice parameter and crystallite size with Cu concentration for various compositions.

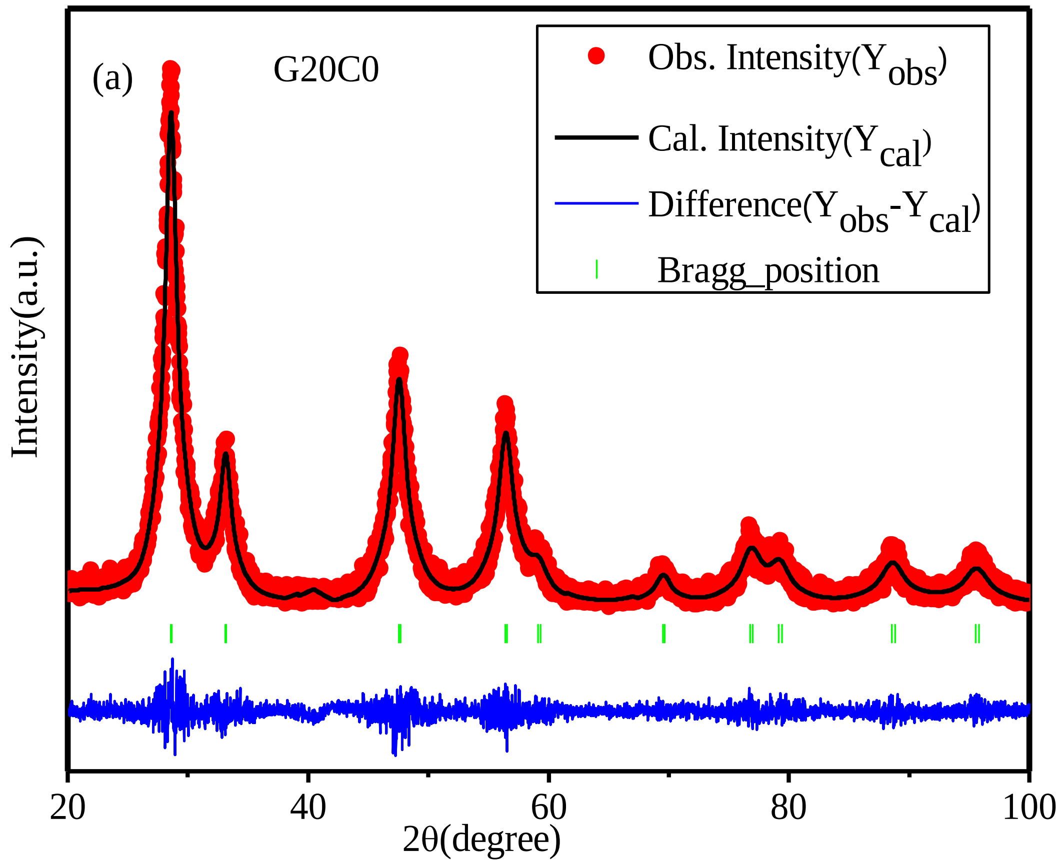

Figure 3.2 (a) Rietveld fits of the X-Ray diffraction patterns of $Ce_{0.8}Ga_{0.2-x}Cu_xO_{2-\delta}$ (x=0.0) The red dots denote experimentally observed data; overlapping black line curve is the Rietveld calculated profile while bottom blue curve denotes the difference plot. Vertical green bars mark the positions of Bragg peaks

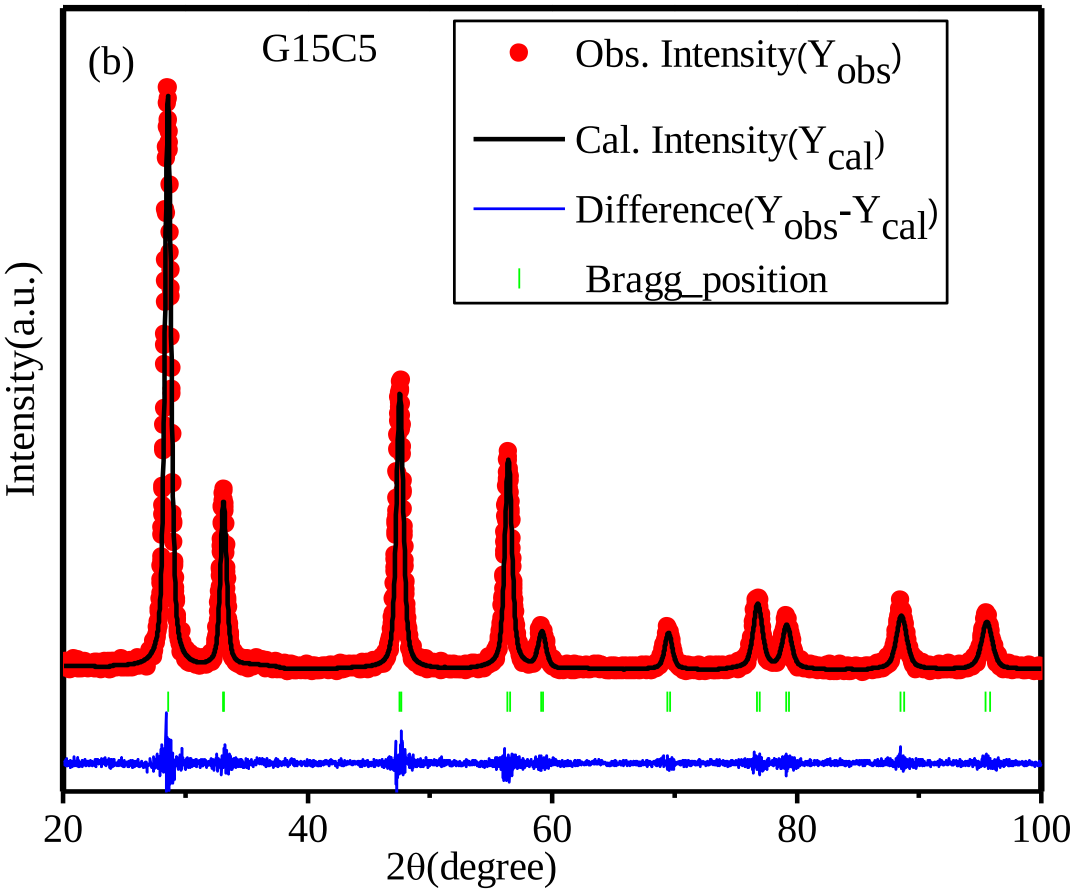

Figure 3.2 (b) Rietveld fits of the X-Ray diffraction patterns of $Ce_{0.8}Ga_{0.2-x}Cu_xO_{2-\delta}$ (x=0.05) The red dots denote experimentally observed data; overlapping black line curve is the Rietveld calculated profile while bottom blue curve denotes the difference plot. Vertical green bars mark the positions of Bragg peaks

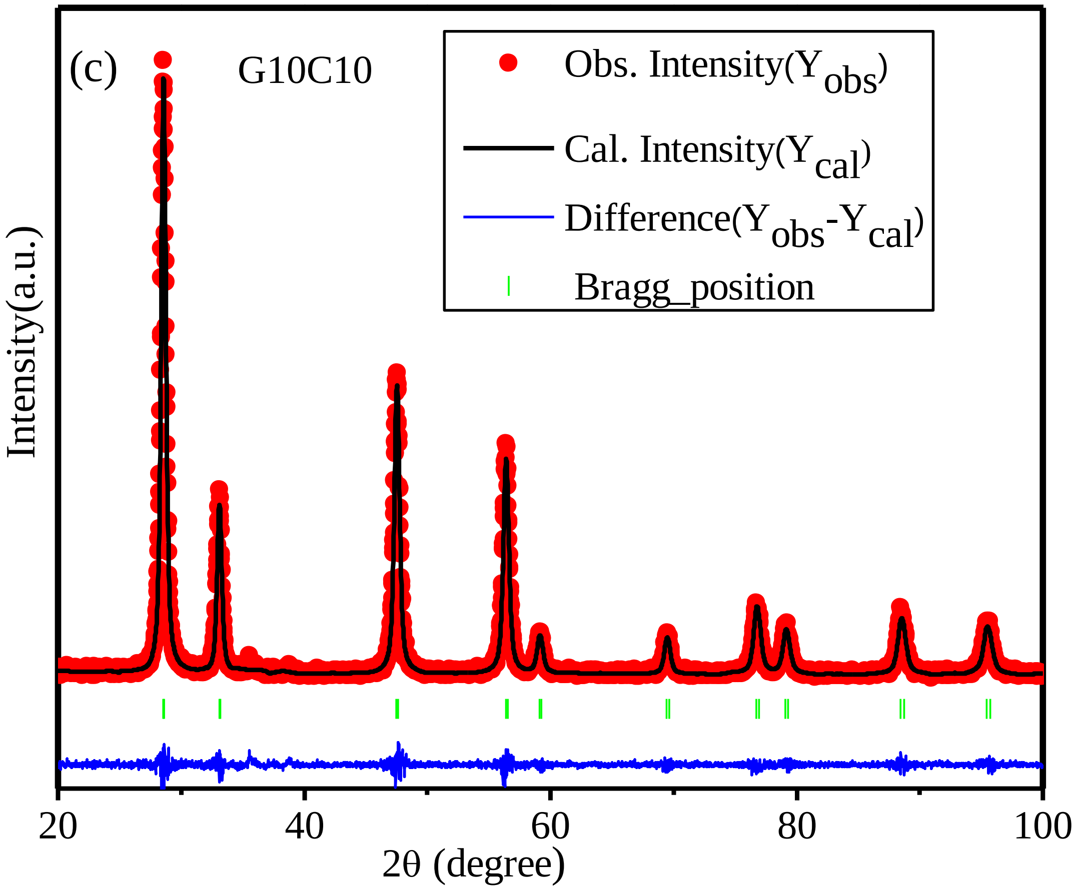

Figure 3.2 (c) Rietveld fits of the X-Ray diffraction patterns of $Ce_{0.8}Ga_{0.2-x}Cu_xO_{2-\delta}$ (x=0.10) The red dots denote experimentally observed data; overlapping black line curve is the Rietveld calculated profile while bottom blue curve denotes the difference plot. Vertical green bars mark the positions of Bragg peaks

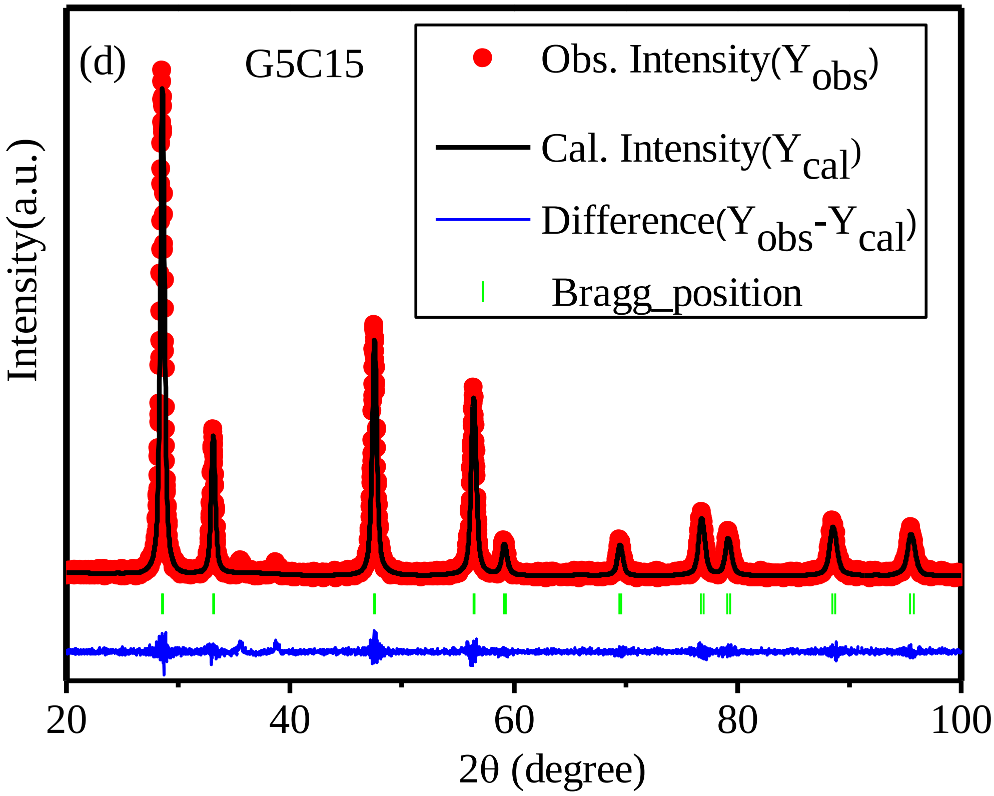

Figure 3.2 (d) Rietveld fits of the X-Ray diffraction patterns of $Ce_{0.8}Ga_{0.2-x}Cu_xO_{2-\delta}$ (x=0.15) The red dots denote experimentally observed data; overlapping black line curve is the Rietveld calculated profile while bottom blue curve denotes the difference plot. Vertical green bars mark the positions of Bragg peaks

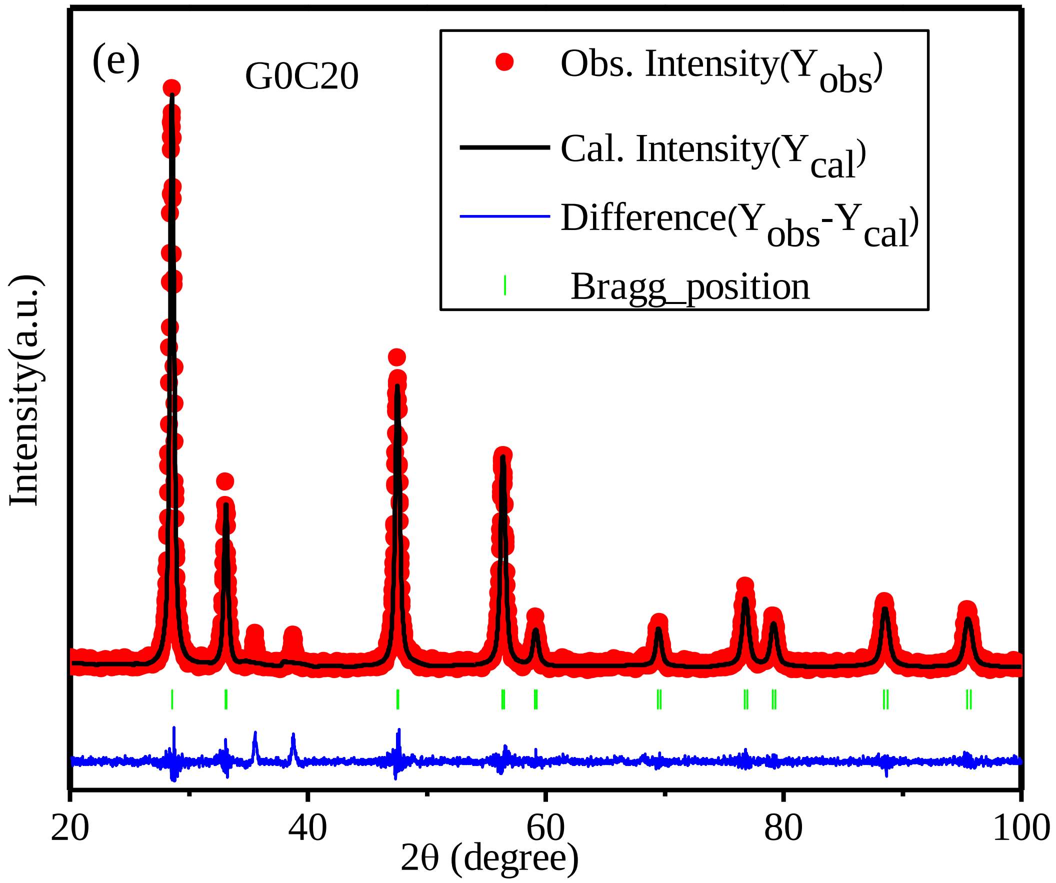

Figure 3.2 (e) Rietveld fits of the X-Ray diffraction patterns of $Ce_{0.8}Ga_{0.2-x}Cu_xO_{2-\delta}$ (x= 0.20). The red dots denote experimentally observed data; overlapping black line curve is the Rietveld calculated profile while bottom blue curve denotes the difference plot. Vertical green bars mark the positions of Bragg peaks.

Table 3.1 Crystallographic and micro-structural information of $Ce_{0.8}Ga_{0.2-x}Cu_xO_{2-\delta}$ samples

Composition	**G20C0**	**G15C5**	**G10C10**	**G5C15**	**G0C20**
Crystal structure	Cubic	Cubic	Cubic	Cubic	Cubic
Lattice parameter (‘a’ Å)	5.4063(4)	5.4087(3)	5.4099(2)	5.4089(2)	5.4097(2)
Volume(Å^3)	158.016(2)	158.2296(3)	158.3299(2)	158.2462(3)	158.3140 (2)
Crystallite size (‘D’ nm)	4	13	17	18	21
Rp	11.9	11.2	11.3	12.1	16.4
Rexp	16.0	16.5	15.9	16.6	16.5
Rwp	17.0	17.3	17.0	17.4	19.2
χ^2	1.1	1.1	1.1	1.1	1.2
RF-factor	1.76	2.22	2.36	2.21	2.84
Relative density(d/d_{th}%)	85.9	90.06	90.2	89.8	89.3

3.3.2 TG/DTA Analysis of the Electrolytes

Figure 3.3 presents a typical TGA/DTA profiles of $Ce_{0.8}Ga_{0.2-x}Cu_xO_{2-\delta}$ (x=0, 0.05 0.1, 0.15, 0.2) solid electrolytes obtained from combustion and without any calcination. The co-doped samples with compositions x = 0.05, 0.10, 0.15, 0.20 exhibit small weight loss up to 800ºC indicating formation of major fraction of the samples during combustion synthesis process itself. The observed weight loss in TGA is ascribed to the decomposition and removal of residual organic byproducts remained in the sample because of incomplete combustion in minor fraction of the samples. It is also observed that weight loss in TGA of the samples decreases with increasing Cu-concentration in various composition (x). Thus CuO co-doping helps in easier formation of electrolytes during combustion. A broad exothermic peak is observed in $Ce_{0.8}Ga_{0.05}Cu_{0.15}O_{1.825}$ which could be correlated to the better crystallization of the sample during thermal treatment. The developed samples also show considerably higher thermal stability among the ceria based solid electrolytes. This is confirmed in simultaneous DTA analysis also as shown in Figure 3.3.

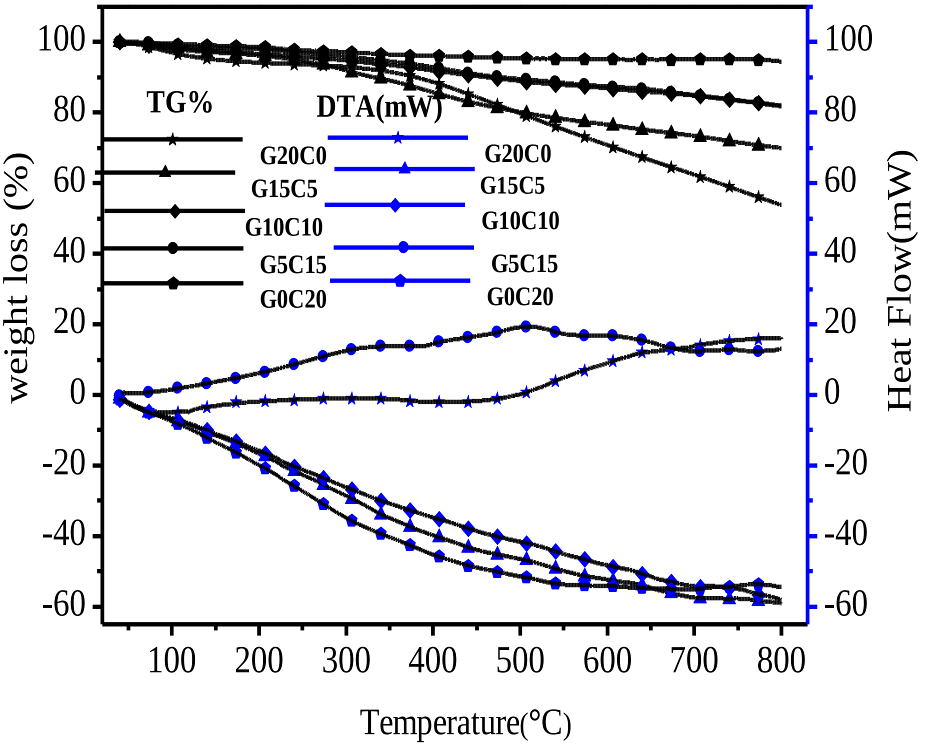

Figure 3.3 TG and DTA profiles of the $Ce_{0.8}Ga_{0.2-x}Cu_xO_{2-\delta}$ (x=0, 0.05, 0.1, 0.15, 0.2) solid electrolytes. The TGA curves for x=0.10 and 0.15 are nearly overlapping.

3.3.3 Raman Spectroscopic Analysis of Electrolytes

To investigate the phase formation and oxygen vacancy confirmation of $Ce_{0.8}Ga_{0.2-x}Cu_xO_{2-\delta}$ (x=0, 0.05, 0.1, 0.15, 0.2) solid solutions, Raman spectroscopy was done on doped ceria samples. Raman spectra of all the compositions calcined at 700°C for 2 hrs are presented in Figure 3.4. The spectrum of pure CeO_2 with fluorite structure is reported to show only one Raman mode of first order positioned around 465 cm^{-1} assigned as F_{2g} symmetry from the fluorite oxygen ion surrounding the Ce^{4+} [Babitha et al., 2015]. As shown in Figure 3.4, for co-doped CeO_2 samples, Raman spectra show a strong peak around 460 cm^{-1} for all the samples which correspond to the triply degenerate Raman F_{2g} vibration peak for fluorite crystal lattice. Apart of the above, emergence of a weak mode around 1160 cm^{-1} indicates the presence of CeO_2 defect as reported by earlier authors also [Lu et al., 2010]. Another broad weak band around 580 cm^{-1} corresponds to the formation of oxygen vacancies in the solid solution as reported earlier also [Peng et al., 2003]. The second peak in Raman spectra corresponding to the oxygen vacancies are not clearly seen in the main panel of the figure. To elaborate it clearly, we have shown the magnified view of second peak shoulder (580 cm^{-1}) in the inset to Figure 3.4 which clearly confirms the creation of oxygen vacancies in the samples. From Figure 3.4, it is found that all the samples have peak shifts towards lower wavelength side as compared to pure ceria which may be due to generation of oxygen vacancies and cell shrinkage. Previously, it was reported that the FWHM value of main ceria line depends strongly on amount of oxygen vacancies in various systems [Babu et al., 2016; Venkataramana et al., 2017]. In view of this, full width at half maxima (FWHM) of the strongest peak was calculated and the results are presented in Table 3.2. The sample with composition $Ce_{0.8}Ga_{0.05}Cu_{0.15}O_{1.825}$ have high value of peak broadening over all the compositions which may be caused by the occurrence of high amount of oxygen vacancies and lower crystallite size in this composition.

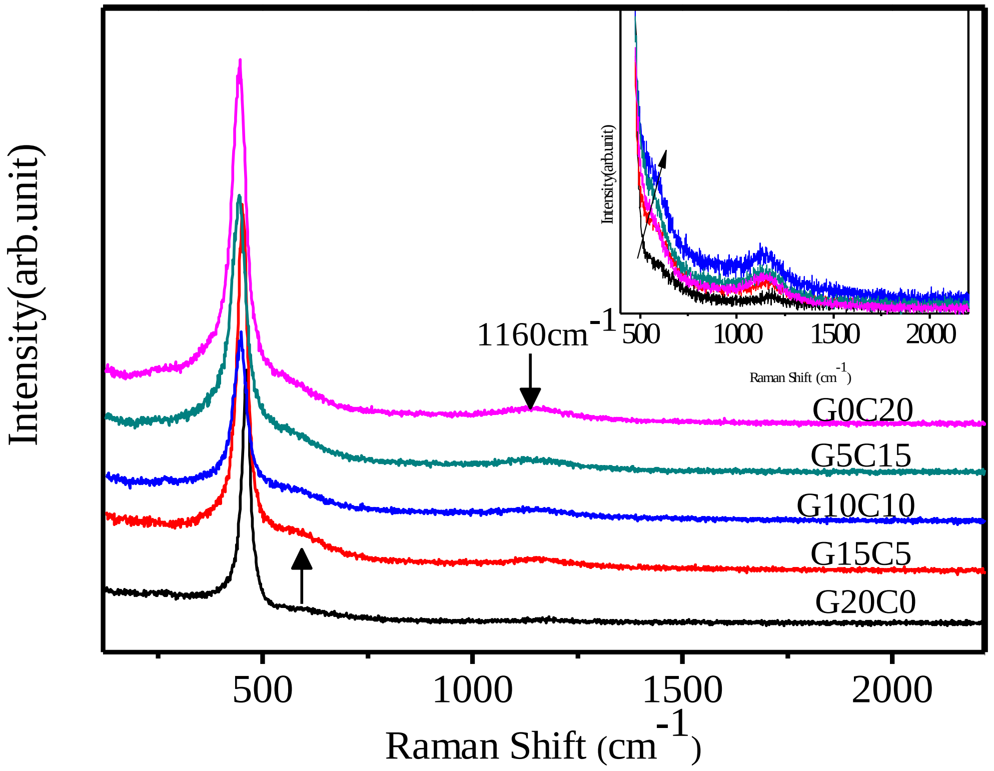

Figure 3.4 Raman spectra of Ce$_{0.8}$Ga$_{0.2-x}$Cu$_x$O$_{2-\delta}$ (x=0, 0.05, 0.10, 0.15, 0.20) calcined at 700°C for 2 hours. Inset gives magnified image of weak bands around 580 cm^{-1} and 1160 cm^{-1} for various compositions.

Table 3.2 List of FWHM value of strongest peak for all compositions.

Samples	**FWHM (cm^{-1})**
G20C0	**27.5**
G15C5	**32.9**
G10C10	**42.8**
G5C15	**45.6**
G0C20	**45.5**

3.3.4 SEM Analysis of Microstructure

The microstructures of the sintered pellets for various compositions, recorded in SEM, are shown in Figure 3.5(a-e). It is evident that the relatively high density is obtained in all the samples. The microstructure shown in Figure 3.5a for 'Ga only' doping exhibits smaller grain size than that for x=0.05 shown in Figure 3.5b. The sintered pellet with 0.05 mol % copper shows the clear precipitation of fine polyhedral shaped grain particles along the grain boundaries and grain size is also enhanced. This confirms that CuO acts as a sintering aid owing to the liquid phase sintering. Upon further increasing the amount of CuO up to the composition x=0.15, the presence of smaller grains due to copper oxide liquid phase increases and form a secondary surface granular phase along with the bigger grains of co-doped ceria in the background. The schematic representation for the CuO precipitates on grain boundaries is given in Figure 3.5f. With further increasing the CuO concentration, the bigger grains of co-doped ceria in the background are covered more showing a partly glassy liquid surface phase. The formation of liquid residues on the surface of the samples for higher CuO concentrations leads to larger size aggregation clusters that’s why the sample with composition x=0.2 possess a slightly lower density as compared to 0.15 mol% Cu^{2+} due to abnormal grain growth. A rapid grain growth occurs due to higher concentration of sintering aid in the G0C20 sample which increases the complexity in the elimination of pore and leads to slightly lower density.

We have performed the EDS analysis on the surface of the samples to confirm further the formation of CuO precipitates in the grain boundary region. The SEM-EDS compositional analysis images for the $Ce_{0.8}Ga_{0.05}Cu_{0.15}O_{1.825}$ sintered pellet from the grain region and grain boundary regions are presented in Figures 3.6 (g, i) and Figures 3.6 (h, j) respectively. The calculated atomic percentages of various atoms are also tabulated in these figures. As can be seen from Figure 3.6i, the calculated atomic percentages of various elements are close to the nominal composition of the sample $Ce_{0.8}Ga_{0.05}Cu_{0.15}O_{1.825}$. However, the EDS spectrum from the grain boundary region given in Figure 3.6j clearly demonstrates that the calculated Cu-concentration is significantly higher than that expected from the nominal composition of the sample. This clearly confirms the segregation of excess CuO precipitates in the grain boundary region.

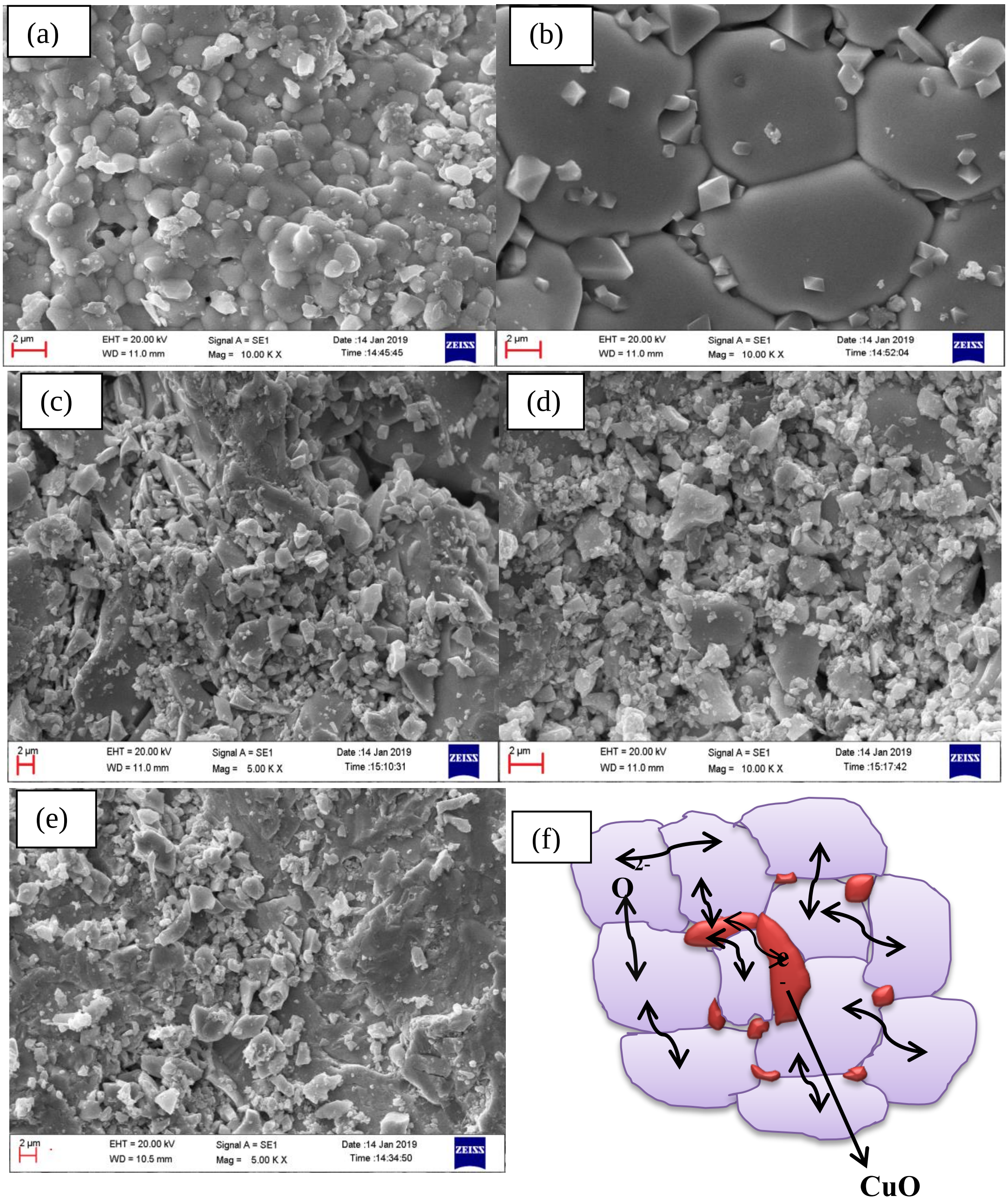

Figure 3.5 (a-d) SEM images of the $Ce_{0.8}Ga_{0.2-x}Cu_xO_{2-\delta}$ (x=0, 0.05, 0.1, 0.15, 0.2) solid electrolytes, (f) schematic micrograph showing CuO precipitates around grain boundaries.

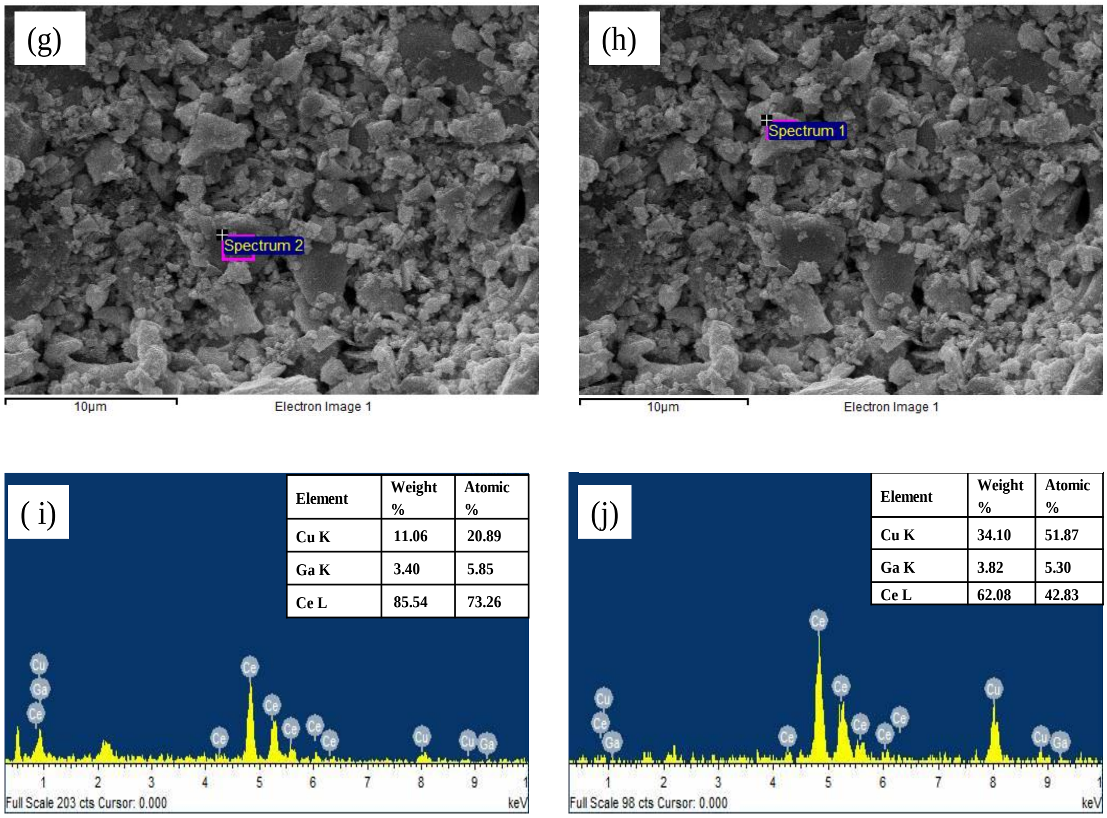

Element	Weight %	Atomic %
Cu K	11.06	20.89
Ga K	3.40	5.85
Ce L	85.54	73.26

Element	Weight %	Atomic %
Cu K	34.10	51.87
Ga K	3.82	5.30
Ce L	62.08	42.83

Figure 3.6 (g, h) SEM images of $Ce_{0.8}Ga_{0.05}Cu_{0.15}O_{1.825}$ and (i, j) corresponding EDS spectrum.

3.3.5 TEM Analysis of the Electrolytes

As shown in the next section, best electrolyte response is obtained in the composition with $Ce_{0.8}Ga_{0.05}Cu_{0.15}O_{1.825}$. In view of this, the TEM studies were done on this composition to get insight into the microstructure of $Ce_{0.8}Ga_{0.05}Cu_{0.15}O_{1.825}$ nanopowder as well as to confirm the crystallite size. Figure 3.7a shows the TEM micrograph of the $Ce_{0.8}Ga_{0.05}Cu_{0.15}O_{1.825}$ nanopowders calcined at 700°C for 2h. It was observed that nano-sized $Ce_{0.8}Ga_{0.05}Cu_{0.15}O_{1.825}$ has very homogeneous distribution of crystallite size and average crystallite size is around ~15nm. The nanocrystallite size derived from TEM image is in well agreement with the size estimated from XRD results. In addition, crystallites are partially agglomerated due to the combustion during high temperature and the corresponding SAED pattern is presented in Figure 3.7c. The observed ring patterns depict good crystallinity of the sample. Indexing of the electron diffraction patterns confirms cubic crystal structure in the F*m-3m* space group and indices of the prominent rings are shown in Figure 3.7c. The lattice fringes in TEM images of nanopowder are clearly resolved in Figure 3.7b with the d-spacing ~0.271 nm which is in a good agreement with the spacing of (200) lattice plane spacing of $Ce_{0.8}Ga_{0.05}Cu_{0.15}O_{1.825}$. Figure 3.7d shows the histogram of the crystallite size which is centered around 15 nm with the Gaussian distribution. This further confirms the uniformity of the microstructure for the prepared electrolyte.

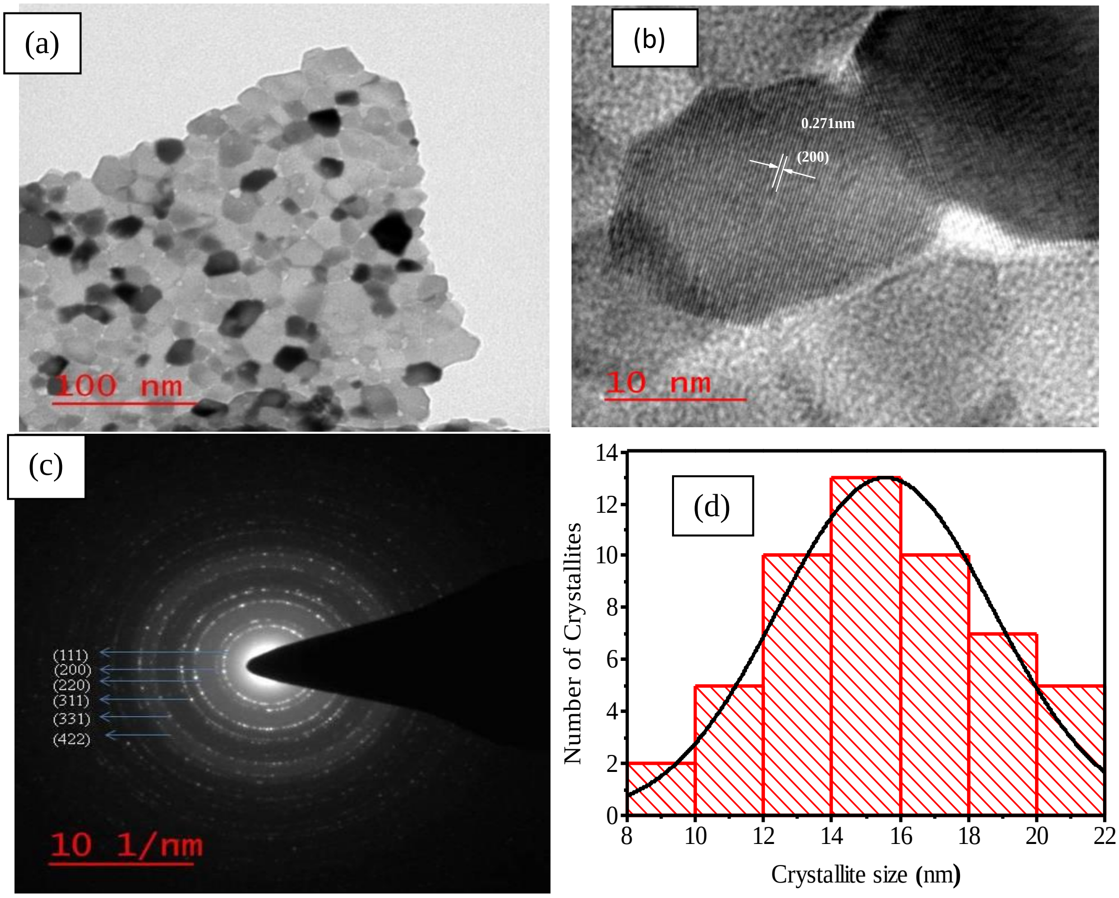

Figure 3.7 (a) TEM micrograph of $Ce_{0.8}Ga_{0.05}Cu_{0.15}O_{1.825}$ (b) high magnification TEM micrograph of the lattice planes, (c) SAED image, and (d) histogram of the distribution of crystallite size of $Ce_{0.8}Ga_{0.05}Cu_{0.15}O_{1.825}$ sample calcined at 700°C for 2 h.

3.3.6 Electrical Characterization of Electrolytes

The ionic conduction properties of the $Ce_{0.8}Ga_{0.2-x}Cu_xO_{2-\delta}$ (x = 0, 0.05, 0.1, 0.15, and 0.2) sintered pellets were done by using impedance spectroscopy over the temperature range of 200°C to 700°C in air for the frequency range of 20Hz-5MHz. Figure 3.8 represents the Nyquist plot for all the co-doped ceria compositions at three different temperatures 600, 650 and 700^{o}C. The typical ionic conduction impedance spectrum consists of three semicircular arcs which correspond to the contribution of grains, grain boundaries, and electrode-electrolyte interfaces in the decreasing frequency order [Anjaneya et al., 2013]. The reason behind the appearance of three distinct arcs is the different time constant for the oxide ion migration along the grains, grain boundaries, and electrode-electrolyte interfaces. As shown in Figure 3.8, as the temperature rises the distinct arcs are getting disappear due to the charge carriers having similar relaxation time for the grain and grain boundary impedance of Ga^{3+}/Cu^{2+} co-doped samples [Ge et al., 2012; Lin et al., 2015]. In contrast, the composition without Cu^{2+} doping retains the contributions from grain and grain boundaries. It is also evident that the electrical conductivity contribution corresponding to the grain boundary conduction is gradually increasing with temperature. The impedance spectra of various compositions have been fitted with equivalent electric circuits consisting of the resistances (R), constant phase element (CPE), and their combinations. The fitted result of Nyquist plots is used to determine the contributions of the resistance from grains (R_g) and the resistance due to grain boundaries (R_{gb}) which was calculated by intersection points of low and high frequency semicircle arcs with the real axis, respectively. For all the co-doped ceria samples, total ionic conductivity was estimated by the equation $\sigma = L/RS$, where L and S denote the thickness and area of the electrolyte pellet, respectively. It is evident from the Table 3.2 that the co-doped samples reveal higher oxide ion conductivity than singly doped compositions which is indication of improvement effect due to co-doping in our system and the sample with composition x=0.15 exhibits the highest ionic conductivity value i.e. 2.03×10^{-2} Scm^{-1} at 700°C. This is due to the segregation of CuO at the grain boundaries which provides additional path for ionic oxygen transportation and thus weakens the space charge effect near the grain boundaries. For further higher doping concentration of Cu^{2+}, the conductivity decreases for the composition x=0.20. The ionic conductivity for the composition with x=0.20 decrease due to higher amounts of CuO liquid phase segregation at grain boundary regions which could create a glassy phase barrier for the oxygen ionic transportation also reported in other systems as well [Lin et al., 2015; Zhou et al., 2009].

The total ionic conduction and ionic conductivity for the solid electrolyte over the temperature range 200°C to 700°C are shown by the Arrhenius plot in Figure 3.9a and 3.9b. The experimental data points for ionic conduction are fitted to the Arrhenius equation: $\sigma_t = (\sigma_o/T) \exp(-E_a/ k_BT)$ to obtain the activation energy (E_a). Here, σ_o is the pre-exponential factor, T stands for absolute temperature, and k_B the Boltzmann constant. The activation energy (E_a) calculated for all the solid electrolytes are enlisted in Table 3.3. It is evident that the composition $Ce_{0.8}Ga_{0.05}Cu_{0.15}O_{1.825}$ exhibits the lowest value of activation energy among all the compositions. The enhanced Cu^{2+} concentration causes the generation of oxygen vacancies and minimizes the association energy between dopant cations and oxygen vacancies leading to high oxygen ion conductivity. The formation of oxygen vacancies due to charge compensation in these oxides can be represented by Kröger-Vink notations as given below:

$$Ga_2O_3 \xrightarrow{2CeO_2} 2Ga_{Ce}^{'} + 3O_O^X + V_o^{\bullet\bullet}$$

$$CuO \xrightarrow{CeO_2} Cu_{Ce}^{''} + O_O^X + V_o^{\bullet\bullet} \qquad \text{Eq. 3.4}$$

The outcome of dopants on the mobility of dense CeO_2 grain boundaries has been observed by earlier authors [Chen et al., 1996]. It has been reported that the potential experienced by an undersized solute is much smaller compared to an oversized solute. Thus diffusivity of the dopant cations can be enhanced by reducing the migration enthalpy. Therefore, the conductivity of the oxide ion in ceria based fluorite type systems can be improved by large mismatch of dopants size with the surrounding lattice. The ionic conductivity of pure ceria is generally not good [Panhans et al., 1993]. Depending on the temperature and partial pressure of oxygen (p_{O2}) ceria also show ionic, p and n-type electronic conductivity. The ionic conductivity contribution decreases and the n-type conductivity increases for ceria with increasing the temperature. Doping of cerium oxide (CeO_2) with lower valence oxides enhance the oxide ion vacancies that improve the oxide ion conduction which makes it suitable as an electrolyte [Mogensen et al., 2000]. The character of ionic conduction in ceramic materials is also established by activation energy values. The activation energies for the oxide ion conduction are typically reported in the range of 0.5-1.0 eV for acceptor doped ceria [Knauth et al., 2002; Zhang et al., 2007]. In case of n-type CeO_2 much lower activation energies, in the range of 0.1-0.2 eV, is reported for Sb-doped CeO_2 ceramics [Neuhaus et al., 2016].

The conduction mechanism in our samples is predominantly ionic, as the activation energies are in the range of 0.62 to 0.83 eV (see Table 3.3), that corresponds to the oxide ion conduction. For electronic conduction, much lower activation energies, in the range of 0.1-0.2 eV are required due to small size of electrons in comparison to oxygen ions.

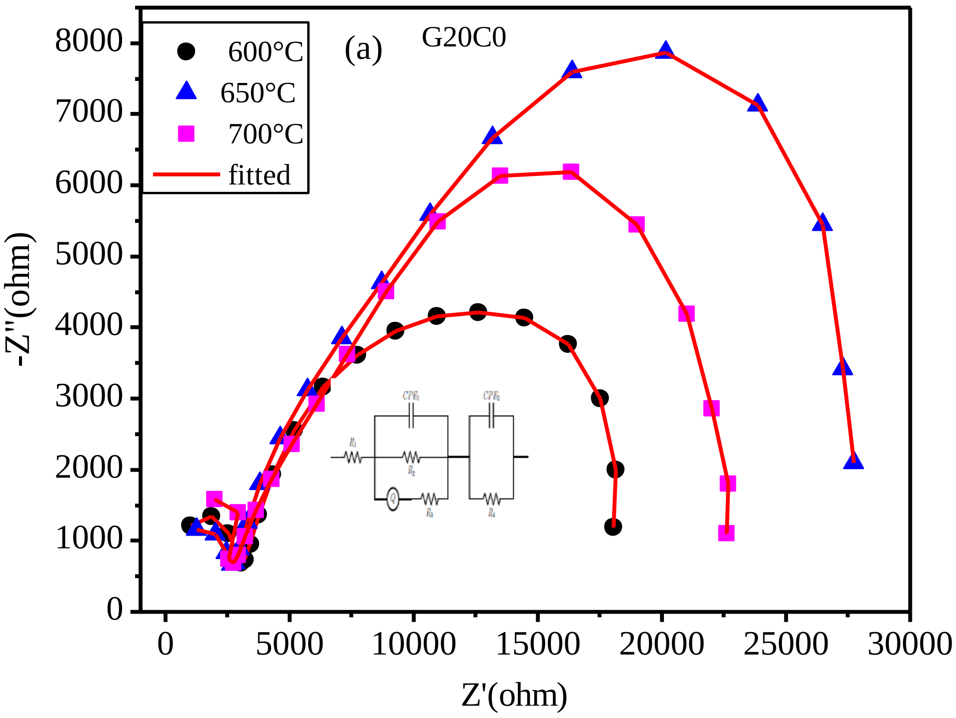

Figure 3.8 (a) Fitted ac impedance spectra of $Ce_{0.8}Ga_{0.2}Cu_{0.0}O_{1.9}$.

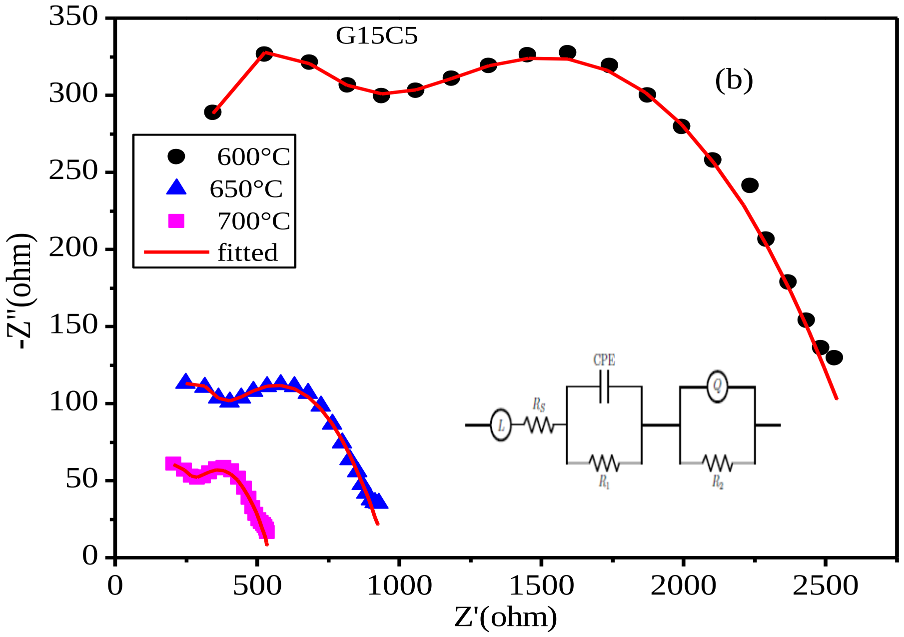

Figure 3.8 (b) Fitted ac impedance spectra of $Ce_{0.8}Ga_{0.15}Cu_{0.05}O_{1.875}$.

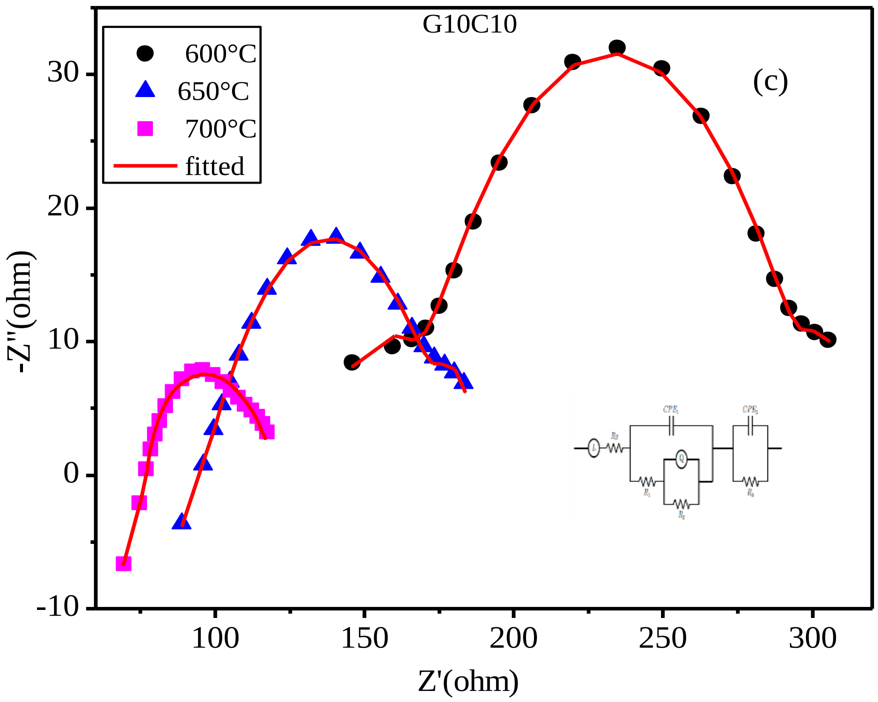

Figure 3.8 (c) Fitted ac impedance spectra of $Ce_{0.8}Ga_{0.10}Cu_{0.10}O_{1.85}$.

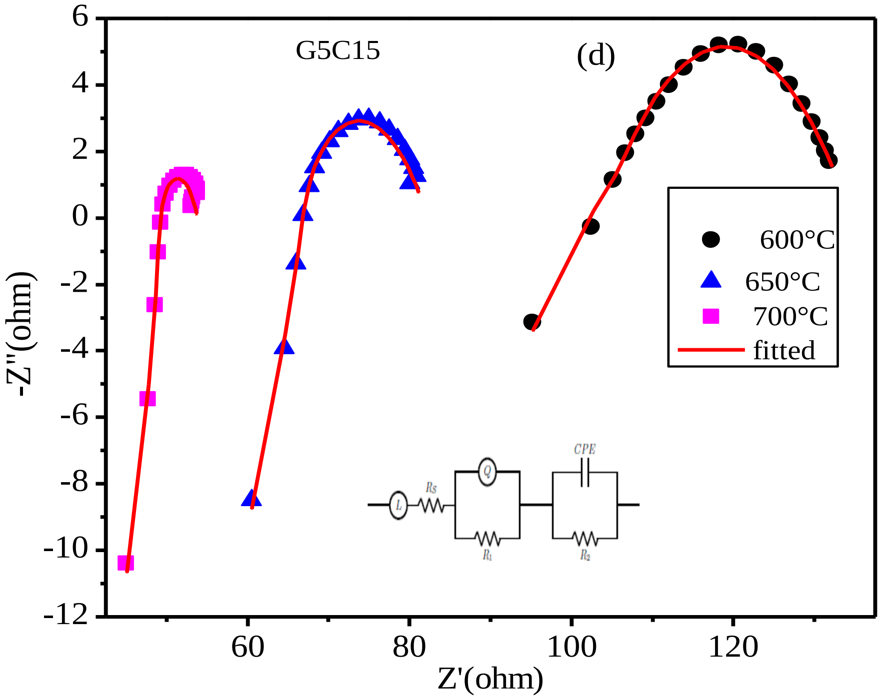

Figure 3.8 (d) Fitted ac impedance spectra of $Ce_{0.8}Ga_{0.05}Cu_{0.15}O_{1.825}$.

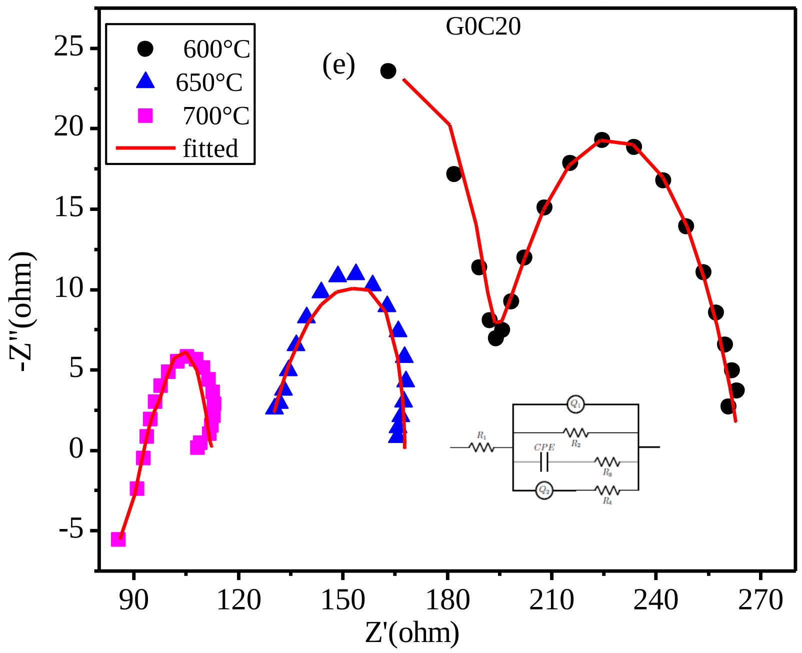

Figure 3.8 (e) Fitted ac impedance spectra of $Ce_{0.8}Ga_{0.0}Cu_{0.2}O_{1.8}$ solid electrolytes sintered at 1300°C.

Table 3.3 Activation energy and total ionic conductivity for $Ce_{0.8}Ga_{0.2-x}Cu_xO_{2-\delta}$ samples.

	Conductivity (S/cm)				
Sl.No.	Sample	600°C	650°C	700°C	E_a (eV)
1	G20C0	5.82×10^{-6}	3.62×10^{-6}	5.04×10^{-6}	0.74
2	G15C5	1.06×10^{-4}	1.85×10^{-4}	2.17×10^{-4}	0.83
3	G10C10	2.32×10^{-4}	3.13×10^{-4}	4.86×10^{-4}	0.66
4	G5C15	8.10×10^{-3}	1.32×10^{-2}	2.03×10^{-2}	0.62
5	G0C20	6.69×10^{-4}	1.0×10^{-3}	1.13×10^{-3}	0.74

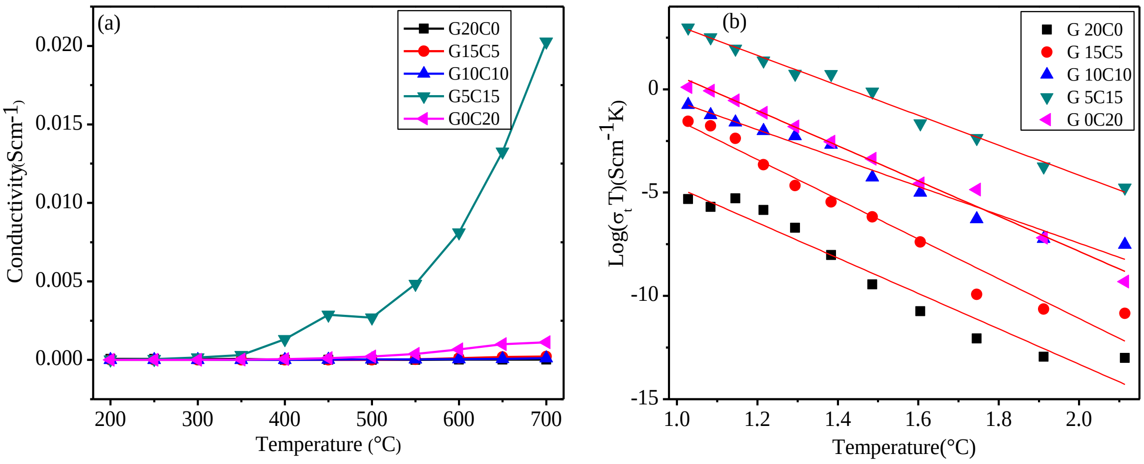

Figure 3.9 (a) Temperature dependence of Ionic conductivity results and (b) Arrhenius plots for $Ce_{0.8}Ga_{0.2-x}Cu_xO_{2-\delta}$ (x=0, 0.05, 0.1, 0.15, 0.2) solid electrolytes in the temperature range 200 to 700 °C.

3.3.7 Thermal Expansion behavior

The thermal expansion coefficient (TEC) of ceria based solid electrolyte material should be comparable to the commonly used cathode and anode materials in order to obtain an efficient electrolyte material. Any mismatch in thermal expansion coefficient can lead to formation of composite micro-cracks at the interfaces of electrode and electrolyte. In view of above, the thermal expansion coefficient of $Ce_{0.8}Ga_{0.05}Cu_{0.15}O_{1.825}$ was determined by using refined lattice parameters obtained from temperature dependent XRD data. The linear thermal expansion (dL/Lo) for the $Ce_{0.8}Ga_{0.05}Cu_{0.15}O_{1.825}$ sample in the temperature range 40- 800°C is presented in Figure 3.10. The TECs values have been estimated from the thermal expansion curves using the equation given below:

$$TEC = \frac{L-L_O/L_O}{T-T_O} \qquad \text{Eq. 3.5}$$

where the initial lattice parameter is L_0, final lattice parameter is L, initial temperature (T_0), and terminal temperature is T. The TEC value of $Ce_{0.8}Ga_{0.05}Cu_{0.15}O_{1.825}$ sample

(11.10×10^{-6} K^{-1}) for 30–800°C is in good consistent with the acceptable range of conventional anode, cathode and electrolyte materials [$(10–13)\times 10^{-6}$ K^{-1}].

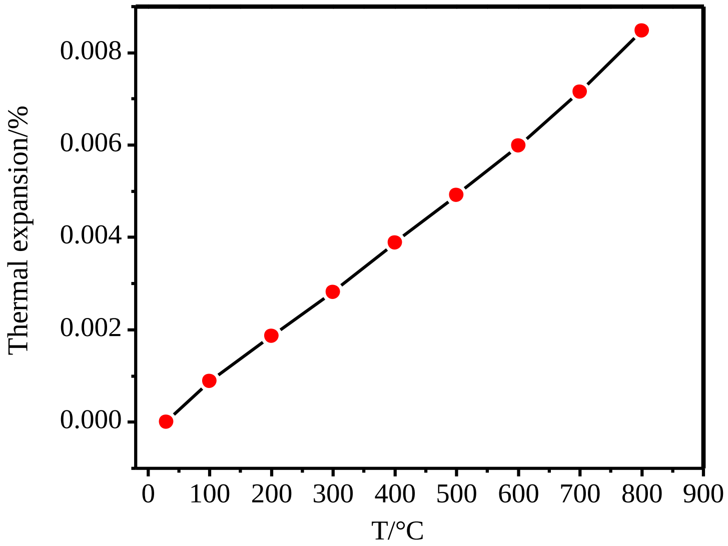

Figure 3.10 Thermal expansion plot of $Ce_{0.8}Ga_{0.05}Cu_{0.15}O_{1.825}$ solid electrolyte.

3.4 Conclusions

In the present study, a novel composition of Ga^{3+} and Cu^{2+} co-doped ceria within system $Ce_{0.8}Ga_{0.2-x}Cu_xO_{2-\delta}$ (for x = 0, 0.05, 0.1, 0.15, and 0.2) have been prepared successfully at low temperatures by using glycine auto combustion synthesis process. The formation of single phase cubic fluorite type crystal structure of all the samples have been confirmed by XRD analysis. In addition, minor second phase precipitate identified as CuO was formed in Cu^{2+} co-doped samples. Rietveld analysis of the XRD data reveals linear variation of the lattice parameters, unit cell volume and crystallite size. The crystallite sizes of the samples increase from 4 nm to 21 nm with increasing Cu^{2+} doping which confirms the liquid phase sintering in the samples. Raman spectroscopic analysis confirms that the composition $Ce_{0.8}Ga_{0.05}Cu_{0.15}O_{1.825}$ shows the highest concentration of oxygen vacancies. The impedance spectroscopy measurement reveals that the $Ce_{0.8}Ga_{0.05}Cu_{0.15}O_{1.825}$ electrolyte sintered for 4 h at 1300°C exhibits the highest ionic conductivity ($\sigma_{700^{o}C} = 2.03\times 10^{-2}$ S cm^{-1}) with least activation energy of conduction (E_a =0.62eV) among all the compositions $Ce_{0.8}Ga_{0.2-x}Cu_xO_{2-\delta}$ investigated. The addition of Cu^{2+} promotes the formation of oxygen vacancies and helps in providing the additional oxygen ion transport path resulting in the superior ionic conductivity. Use of the developed materials as solid electrolyte for potential application in IT-SOFC will reduce the cost significantly. From overall results, we conclude that the co-doped ceria ceramic material $Ce_{0.8}Ga_{0.05}Cu_{0.15}O_{1.825}$ would be a better choice as an efficient electrolyte in IT-SOFCs.